UC San Diego
Oceanography Program Publications

Title
Regional Swell Transformation by Backward Ray Tracing and SWAN

Permalink
https://escholarship.org/uc/item/8tv4w9g3

Journal
Journal of Atmospheric and Oceanic Technology, 36(2)

ISSN
0739-0572 1520-0426

Authors
Crosby, Sean C
Kumar, N.
O'Reilly, W. C
et al.

Publication Date
2019-02-01

DOI
10.1175/JTECH-D-18-0123.1

Data Availability
The data associated with this publication are available upon request.

Peer reviewed

Regional Swell Transformation by Backward Ray Tracing and SWAN

SEAN C. CROSBY

Western Washington University, Bellingham, Washington

N. KUMAR

Department of Civil and Environmental Engineering, University of Washington, Seattle, Washington

W. C. O'REILLY AND R. T. GUZA

Integrative Oceanography Division, Scripps Institution of Oceanography, La Jolla, California

ABSTRACT

Beach erosion and wave-induced flooding models are often initialized in $O(10)$-m depth, seaward of the surfzone, with wave conditions estimated from regional nonlinear spectral wave models [e.g., Simulating Waves Nearshore (SWAN)]. These models are computationally expensive for high-resolution, long-term regional $O(100)$-km hindcasts, and they limit examination of the effect of different climate scenarios on nearshore processes. Alternatively, computationally fast models with reduced linear wave physics enable long-term hindcasts at high spatial (<100 m) resolution. Linear models, that efficiently transform complete spectral details from deep water through complex offshore bathymetry, are appropriate for low-frequency swell wave energy propagation. Here, two numerically different linear methods are compared: backward ray-tracing and stationary linear SWAN simulations. The methods yield similar transformations from deep water (seaward of offshore islands in Southern California) to the nearshore, $O(10)$-m depth. However, SWAN is sensitive to model spatial resolution, especially in highly sheltered regions, where with typical (1–2 km) resolution SWAN estimates of nearshore energy vary by over a factor of 2 relative to ray tracing. Alongshore radiation stress estimates from SWAN and ray tracing also differ, and in some cases the climatological means have opposite signs. Increasing the SWAN resolution to 90 m, higher than usually applied to regional models, yields the nearshore transforms most similar to ray tracing. Both accurate rays and high-resolution SWAN require significant computation time; however, ray tracing is more efficient if transforms are needed at relatively few locations (compared with every grid point), or if computer memory is limited. Though presently less user friendly than SWAN, ray tracing is not affected by numerical diffusion or limited by model domain size or spatial resolution.

1. Introduction

Surface gravity waves often dominate nearshore circulation and mixing, and additionally erode beaches and force high water levels that threaten coastal infrastructure. Waves drive alongshore sediment transport for which accurate predictions depend critically on high-resolution energy and directional (e.g., alongshore radiation stress) wave information at the shoreline (Komar and Inman 1970). Nonlinear models describing details of shallow-water wave shoaling, breaking, and runup run at relatively high resolution in space [$O(1)$ m] and time [$O(1)$ s; e.g., Rijnsdorp et al. 2014]. These models are often initialized seaward of the surfzone (between 8- and 30-m depth) with nearshore sea-swell waves, estimated with regional nonlinear spectral wave models that include refraction, shoaling, blocking by islands and capes, wind generation, nonlinear wave interactions, bottom friction, and other source terms [e.g., Simulating Waves Nearshore (SWAN); Booij et al. 1999]. Lagrangian (ray following) approaches (Ardhuin et al. 2001, 2003a,b) reduce the computational burden. However, fully nonlinear spectral models are inherently computationally expensive and presently impractical for high-resolution, long-term regional $O(100)$-km hindcasts and for examining the

effect of climate scenarios on regional waves (Menéndez et al. 2008; Young et al. 2011). Alternative statistical and hybrid approaches have been developed for regions with one (Camus et al. 2011) and multiple wave sources (Hegermiller et al. 2017; Portilla-Yandún et al. 2015). However, hybrid approaches are limited to bulk descriptions (e.g., significant wave height, peak period, mean direction) of wave conditions, or bulk descriptions of each wave partition, and may lack spectral details critical to initializing models for surfzone processes (Crosby et al. 2016; Kumar et al. 2017).

The approach pursued here uses reduced linear wave physics to efficiently transform complete swell directional spectra from offshore deep water (the domain of global low-resolution models) to the nearshore (e.g., Southern California; Fig. 1). Over relatively short (100 km) scales, swell wave propagation is nearly linear. For example, along the U.S. West Coast, swell ($\leq 0.09\,\mathrm{Hz}$) arriving from distant storms propagates approximately linearly through the islands and across the shelf (O'Reilly and Guza 1991; Crosby et al. 2016). Buoy observations offshore of the islands are used to initialize hourly real-time linear wave transformations to the 10-m (or 15-m)-depth contour at 100-m (or 200-m) alongshore resolution for all of coastal California [Coastal Data Information Program (CDIP); http://cdip.ucsd.edu/; O'Reilly et al. 2016]. Additionally, linear wave transformations allow relatively computationally rapid assimilation of regional and nearshore observations into regional models (O'Reilly and Guza 1998; Crosby et al. 2017).

Wave incidents on the Southern California Bight (SCB) are dominated by low-frequency ($\leq 0.09\,\mathrm{Hz}$) swell arrivals from the North Pacific, mixed with seasonally important South Pacific swell (Fig. 2). Mean offshore spectra predictions $\overline{E_o(f, \theta_o)}$ at the Harvest, California, buoy from the National Oceanic and Atmospheric Administration's WaveWatch III hindcast (NOAA-WW3 hindcast; Tolman 2009; Chawla et al. 2011, 2013) illustrate this bimodal swell energy arrival (Fig. 2). Owing to the wide range of incident deep-water wave directions, and the complex offshore island and shoal bathymetry, the nearshore wave field varies widely in space and time. Previous studies illustrate the sensitivity of sheltered waves to spectral offshore boundary conditions (Crosby et al. 2016; Kumar et al. 2017), stationary and nonstationary assumptions, and model spatial resolution (Rogers et al. 2007). Nonlinear spectral models are computationally demanding, and regional model grid resolution is historically coarse (2–5 km; Rogers et al. 2007). However, increasing grid resolution (e.g., 500 m; Kumar et al. 2017; Gorrell et al. 2011) does not necessarily resolve island and shelf bathymetry (Fig. 1).

Regional and nearshore transformation coefficients are derived from linear models that include refraction, shoaling, and island blocking. Two approaches (described in section 2) are compared: the commonly used model SWAN (with nonlinear and source/sink terms turned off), and the less frequently applied backward ray tracing. SWAN simulations are inherently more numerically diffusive, though higher-order numerics do reduce numerical diffusion. Previously, Rogers et al. (2002) developed higher-order numerics for SWAN and compared these with ray-derived predictions and observations in the Santa Barbara Channel. Skill was highest for ray-derived predictions, followed by second- and first-order SWAN solutions. Here, we extend Rogers et al. (2002) by testing SWAN for a large range of spatial resolutions, and for wave radiation stress and angle as well as energy. As discussed in section 3, the models produce qualitatively similar transfer functions; however, the SWAN results are sensitive to spatial resolution. Additionally, differences in computation strategy make ray tracing more efficient if transforms are needed at relatively few locations (compared with every grid point), or if computer memory is limited. Findings are summarized in section 4.

2. Methods

Under linear assumptions phase-averaged wave energy at the nearshore E_n can be related to offshore wave conditions E_o, such that

$$E_n(i,t,f) = \int K(i,f,\theta_o) E_o[f, \theta_o, t - \tau(i,f,\theta_o)] \, d\theta_o \quad (1)$$

at nearshore location i, time step t, frequency f, and integrated over offshore directions θ_o (O'Reilly and Guza 1991, 1993). Transformation coefficients K are applied to offshore energy lagged by τ, the frequency–directional-dependent travel time for location i. When model time steps are larger than travel times, (1) simplifies with $\tau = 0$. Here, for simplicity travel time is not considered; however, previous studies have applied time lags to this linear transformation (O'Reilly and Guza 1998; O'Reilly et al. 2016; Crosby et al. 2017). Additionally, in (1) wave energy offshore is assumed homogeneous in the direction perpendicular to travel, a valid assumption for low-frequency wave energy offshore of Southern California (appendix A of Crosby et al. 2016).

Coefficients in K are a function of refraction, shoaling, and sheltering between a nearshore location and an offshore boundary. Estimation of these coefficients can be computationally costly; however, once derived, predictions are quickly generated from the straightforward integral in (1). Here, two approaches to estimate K are
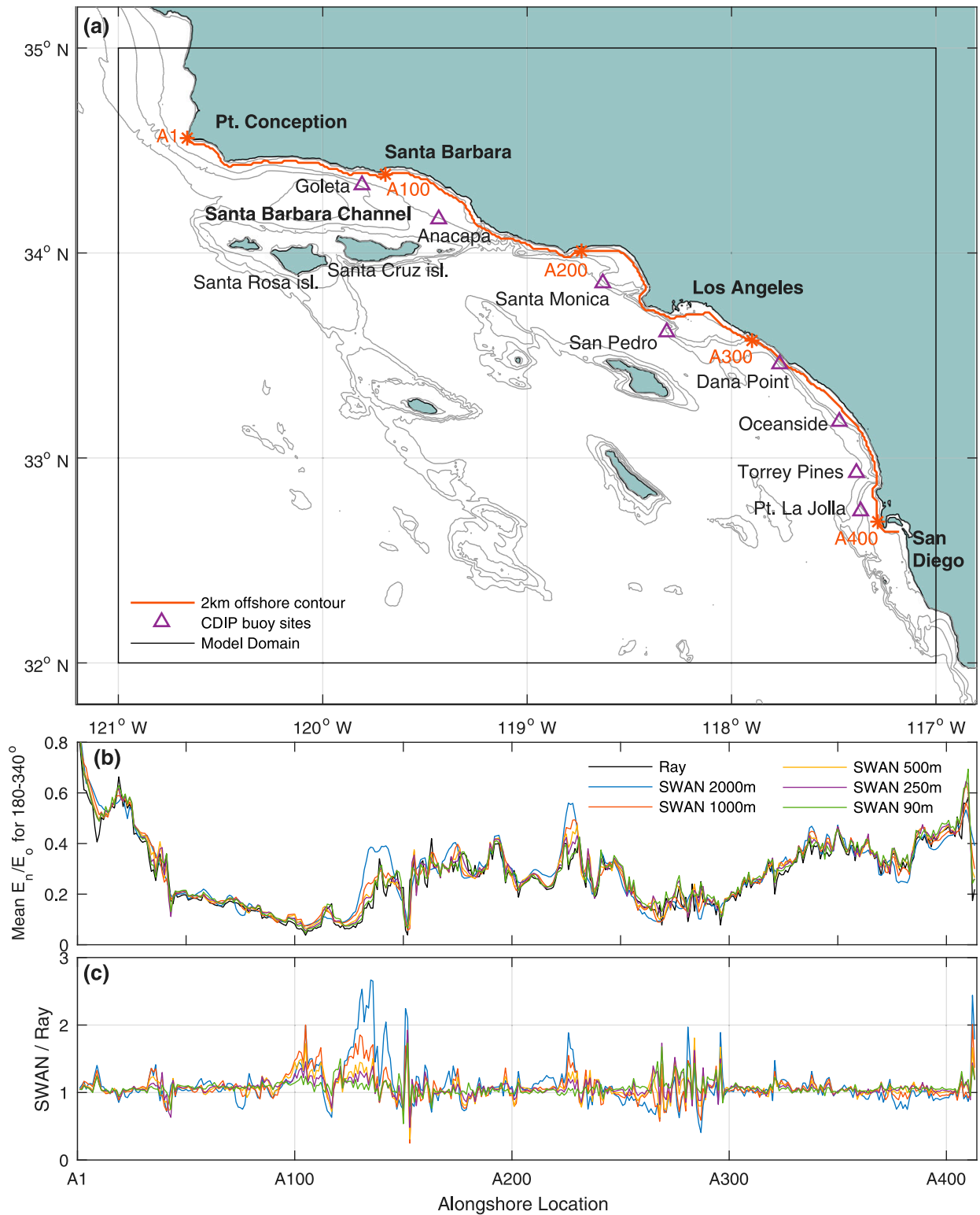
FIG. 1. (a) SCB model domain (black box), nominally 50-m-depth alongshore contour (red), and operational CDIP buoy sites (magenta triangles). Gray contours show 20-, 50-, 2000-, and 500-m isobaths. (b) Energy transform coefficients estimated at the 50-m-depth contour for incident energy arriving from 180° to 340° at 0.07 Hz. Transform coefficients (ratio of arrival energy to incident offshore energy) are derived from backward ray tracing (black) and stationary SWAN simulations at varying spatial resolutions (colors). (c) Ratio of SWAN-derived to ray-derived coefficients.
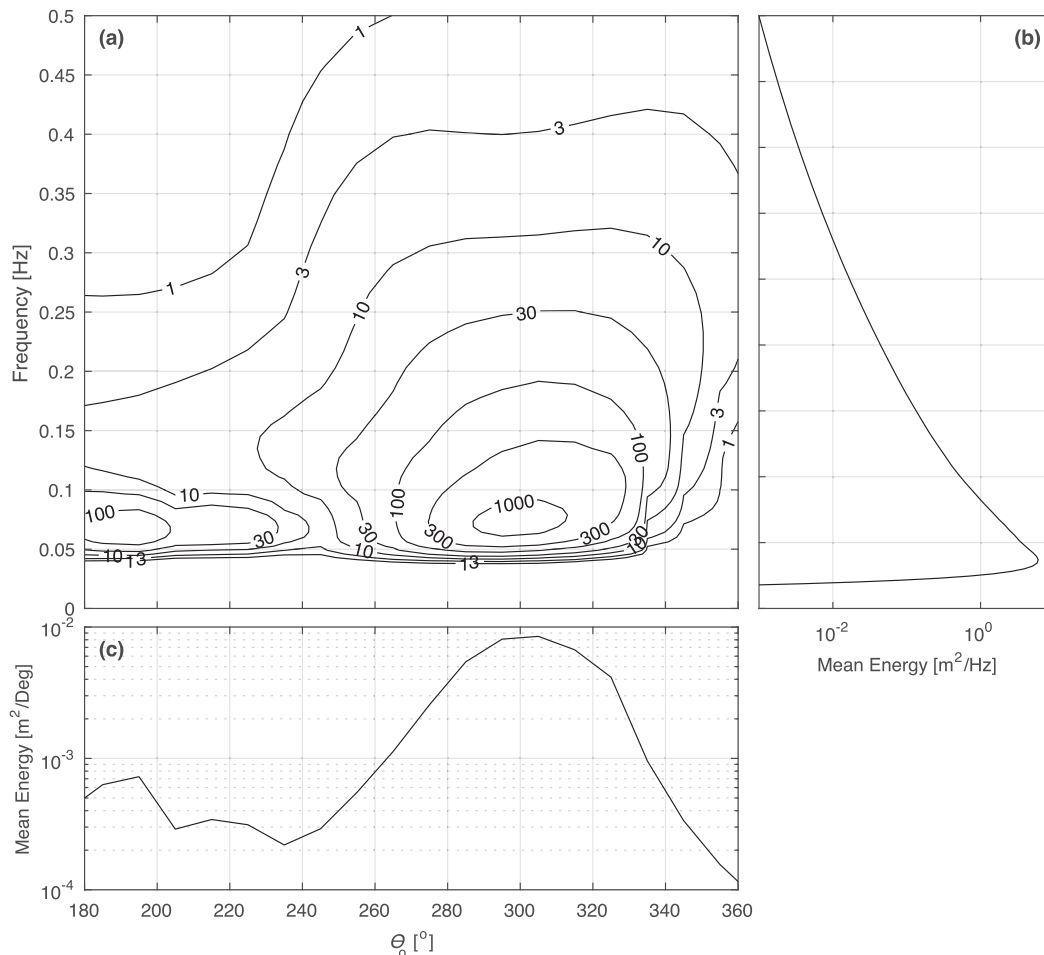
FIG. 2. (a) Mean wave energy $\overline{E_o(f, \theta_o)}$ contours (log scale) vs frequency and direction, derived from the 2000–09 NOAA-WW3 CFSR predictions at Harvest buoy site. (b) Mean energy vs frequency integrated in direction and (c) mean energy vs direction integrated in frequency.

compared: SWAN simulations and backward ray tracing. Bathymetry input for both methods is from the NOAA-NGDC Coastal Relief Model (https://www.ngdc.noaa.gov) at 90-m spatial resolution.

a. Ray tracing

The transfer coefficients in K are estimated by backward ray tracing under the assumption that bathymetry varies slowly relative to wavelength (Longuet-Higgins 1957; Dorrestein 1960; Le Mehaute and Wang 1982). At each frequency f and nearshore site i, rays are traced, beginning from varying nearshore directions θ_n to deep water offshore. From available bathymetry phase velocity gradients are estimated with second-order polynomial interpolation, and used with a fifth-order Runge–Kutta numerical scheme and varying temporal step size to integrate the Cartesian ray equations,

$$\frac{dx}{dt} = c\cos\alpha, \quad \frac{dy}{dt} = c\sin\alpha, \quad \frac{d\alpha}{dt} = \frac{dc}{dx}\sin\alpha - \frac{dc}{dy}\cos\alpha,$$

(2)

where x and y specify ray position, and α and c specify ray angle and local phase speed, respectively (O'Reilly and Guza 1993). The error threshold in the Runge–Kutta algorithm, that controls step size, was reduced until ray path differences were much less than the bathymetry resolution (90 m). Strict error tolerances impacted computational cost minimally. Rays in spherical (Munk et al. 1988) and Cartesian coordinates (used here) yielded negligibly different K for Southern California.

Rays striking land (depths < 10 m) are terminated, and these nearshore directions are considered blocked. Rays extending beyond nearshore islands and into deep water (depths > 500 m) are considered unblocked directions. From geometric optics the relationship between

onshore and offshore angles of adjacent unblocked rays determines K, such that

$$K[i, f, \theta_o, g(\theta_n)] = \frac{k^{(n)}(f)}{k^{(o)}(f)} \frac{c_g^{(o)}(f)}{c_g^{(n)}(f)} \int \left| \frac{\Delta\theta_n}{\Delta\theta_o} \right| g(\theta_n)\, d\theta_n, \quad (3)$$

where $c_g^{(n)}$ and $c_g^{(o)}$ are group velocities; and $k^{(n)}$ and $k^{(o)}$ are wavenumbers at nearshore (n) location i and offshore (o) ray termination site, respectively (Dorrestein 1960; Le Mehaute and Wang 1982). Terms $\Delta\theta_n$ and $\Delta\theta_o$ indicate the difference in starting and ending ray angles of adjacent rays (adjacent referring to rays starting at adjacent nearshore angles), respectively. Here, the function $g(\theta_n)$ is included to expand the transformation in (1) to directional information; for example, if $g(\theta_n) = \sin 2\theta_o$, then K transforms the coefficient for the b_2 directional moment observed by a directional wave buoy (Longuet-Higgins et al. 1963) and related to the radiation stress S_{xy}. When $g(\theta) = 1$, (3) simplifies and (1) transforms total energy. Example ray tracing and subsequent integrations to form K are in O'Reilly and Guza (1991, 1998).

The density of rays traced is determined iteratively to maintain computational efficiency while resolving accurately the relationship between $\Delta\theta_n$ and $\Delta\theta_o$ in regions with complex bathymetry. After an initial sweep through θ_n at 0.5° increments, rays are bisected where adjacent terminating angles are greater than 1° and at blocked–unblocked junctions, until terminating angle differences are less than 1°, or the θ_n resolution is less than either 0.1° or $0.1(k_n/k_o)(C_g^{(o)}/C_g^{(n)})$. Each ray is independent and parallelization is simple.

As part of CDIP's prediction system, transform coefficients were derived for the following: 1) all buoy locations in the SCB for model validation; 2) alongshore locations with approximately 100-m spacing in 10-m depth for nearshore process modeling; and 3) region-wide locations with uniform 0.01° (1 km) and 0.001° (100 m) latitude–longitude spacing, in water depths greater than and less than 60 m, respectively, to create regional wave maps (http://cdip.ucsd.edu). Rays were traced at a frequency resolution of 0.001 Hz. Subsequently, transfer coefficients were integrated across θ_n and discretized at 5° resolution in θ_o. Then K was averaged across frequency to a 0.01-Hz resolution, comparable to the resolution of boundary observations or global wave model output. Here, CDIP-derived transform coefficients are compiled at buoy sites and alongshore from the U.S.–Mexico border to Point Conception, California (Fig. 1a) and are compared with SWAN. The selected locations illustrate alongshore variability about 2 km from land in ~50-m depth (as deep as 400 m at submarine canyons).

b. SWAN

SWAN, a third generation, phase-averaged wave model solving the wave action balance (Booij et al. 1999), is widely used in regional and local wave simulations. SWAN includes shoaling, wave refraction resulting from both bathymetry and mean currents, diffraction, energy input from wind, triad and quartet interactions, energy loss resulting from whitecapping, bottom friction, and depth-limited breaking. Here, nonlinear and higher-order physics are disabled, such that SWAN includes bathymetric refraction and shoaling, and depth-limited breaking. Diffraction is an important term, especially in the shadow of offshore islands; however, SWAN models diffraction poorly at typical resolutions (obstacle resolution must be ~1/10 of a wavelength), and previous studies suggest that diffractive effects are masked by offshore directional spreading (O'Reilly and Guza 1991, 1993). Dissipation by bottom friction is neglected because it is minimal on the narrow SCB shelf (O'Reilly et al. 2016). Spherical model coordinates are regularly spaced over the SCB extending between 32° and 35°N and between 117° and 121°W (Fig. 1a). Energy spectra are modeled with a directional resolution of 2° and eight frequency bins spaced logarithmically between 0.05 and 0.09 Hz. Offshore spectra, uniform in frequency with all energy at narrow 2° directional bins, are applied to southern, western, and northern boundaries. Energy is normalized to 1-m offshore wave height. Stationary SWAN is run for offshore directions varying from 180° to 360° in 2° increments.

Convergence of simulations with the present very narrow spectra was confirmed. By default, SWAN stops if wave height differences between iterations are less than 0.005 m or if relative change is less than 1% at 99.5% of grid cells. Results were similar (within 0.5%) with more stringent settings (wave height changes less than 0.0025 m, or relative change is less than 0.5% at 99.8% of grid cells). Additionally, the number of iterations never reached the allowed maximum (50).

In stationary mode SWAN employs second-order upwind (SORDUP) numerics (Rogers et al. 2002) by default. Owing likely to directionally narrow incident energy in SCB simulations, the garden-sprinkler effect (GSE) was apparent with SORDUP numerics and was the strongest leeward of offshore islands. Increasing direction resolution (from 2°) to correct this was impractical, especially at high spatial resolution. Alternatively, simulations with more diffusive first-order numerics, backward space backward time (BSBT), were robust without evidence of the GSE. However, despite numerical GSE artifacts, second-order numerics were most similar to ray solutions and are used here.

Transform coefficients are estimated from modeled spectra at each offshore direction and frequency, such that

$$K[i,f,\theta_o,g(\theta_n)] = \frac{\int E_n(f,\theta_n)g(\theta_n)\,d\theta_n}{E^{BC}(f,\theta_o)}, \qquad (4)$$

where E^{BC} is the offshore spectra.

Model simulations with spatial resolutions of 2 km, 1 km, 500 m, and 250 m could be run on a typical desktop computer. Simulations at 90 m required additional memory and several days on a cluster. Significantly larger model simulations—that is, increased spatial, directional, or frequency resolution—may be impractical at the present time.

c. Model boundaries

Model boundaries that include a shallow shelf (upper-left and lower-right corners in Fig. 1) are often difficult to specify accurately. Energy arrivals at high angles—that is, near parallel to the coastline—are often a function of bathymetry outside the domain. For example, south of the SCB the southern extent of Baja California's irregular coastline and offshore islands may or may not block incoming energy where $\theta_o < 180°$ and, similarly, the northern boundary near Point Conception may be partly sheltered by the coastline farther north where $\theta_o > 320°$.

Uniform energy is applied to all SWAN simulation boundaries. To compensate for errors arising from shoaling and refraction near the shore and unmodeled sheltering from bathymetry outside the domain, the model is extended slightly northward and southward. Similar uncertainties occur when rays traveling nearly perpendicular to the coastline leave the domain and become difficult to characterize as blocked or unblocked. CDIP's methodology includes a depth cutoff for classification; rays leaving the domain at depths $\leq$ 300 m are considered blocked. Here, analysis of transfer coefficients was limited to $180° \leq \theta_o \leq 340°$ to avoid these boundary uncertainties.

3. Results and discussion

SWAN simulations and ray-tracing model the same physics of shoaling and refraction, and in theory yield equal transfer coefficients. However, the two approaches are numerically different. Ray tracing uses simple optics and depends on the accurate integration of (2) and sufficient resolution of the relation between nearshore and offshore ray angles. SWAN relies on the stability and accuracy of implicit numerics and is inevitably limited in resolution (space, direction, and frequency) by computational constraints. Given accurate bathymetry, ray-tracing techniques provide an accurate estimate of refraction and shoaling (provided ray integration convergences, and sufficient rays are traced), where SWAN numerics always suffer from some numerical diffusion.

Overall, SWAN- and ray-derived energy transfer coefficients are similar; for example, Fig. 1b shows the nearshore energy transfer coefficient for 0.07 Hz, averaged over the entire open directional aperture, 180°–340°. However, in the east end of the Santa Barbara Channel, near alongshore locations A110–A130, coarse (2000, 1000 m) SWAN coefficients are 1.5–2.5 times larger than ray-derived estimates (Fig. 1c). In Santa Monica Bay, near A225, and along the Los Angeles coast differences approach 1–2 times larger or smaller. In most cases it appears that coarser SWAN model estimates overpredict energy transfer in highly sheltered regions (Fig. 1c). Overall, increasing the spatial resolution of SWAN tends to improve the agreement between SWAN- and ray-derived methods.

SWAN-derived transforms are smoother than rays, even at high resolution (90 m; Figs. 3a,b). The relatively rough features in ray-derived transforms likely represent actual refraction patterns, although realistic incident directional spread usually masks these fine details (O'Reilly and Guza 1993). Despite differences (Fig. 3c), the overall sheltering pattern in the region (Figs. 3a,b) and the mean energy transformation (Fig. 3d) are similar between methods. Higher-resolution SWAN results tend to be more similar to ray-tracing results; however, at offshore directions < 240° ray-tracing estimates are slightly lower (Fig. 3d). Additionally, at offshore directions > 300°, and locations A1–A40, ray-derived transforms are much lower than SWAN. Likely, uniform energy imposed on the northern SWAN boundary incorrectly introduces energy at sharp northwest angles that would otherwise be blocked by the coastline farther north (see section 2c). In contrast, rays terminating on the shelf offshore of Point Conception may be incorrectly classified as blocked, resulting in lower-than-expected energy arrival. One or both boundary concerns may account for the discrepancy in northwest transform coefficients, highlighting the need for careful consideration of the model boundary.

Historically, agreement between wave models and observations in the Santa Barbara Channel is poor compared with farther south (Rogers et al. 2007; O'Reilly et al. 2016; Crosby et al. 2016, 2017). The channel shoreline is highly sheltered and energy arrival is complex, with sometimes rapid alongshore variation. For example, waves from the west creates several relative
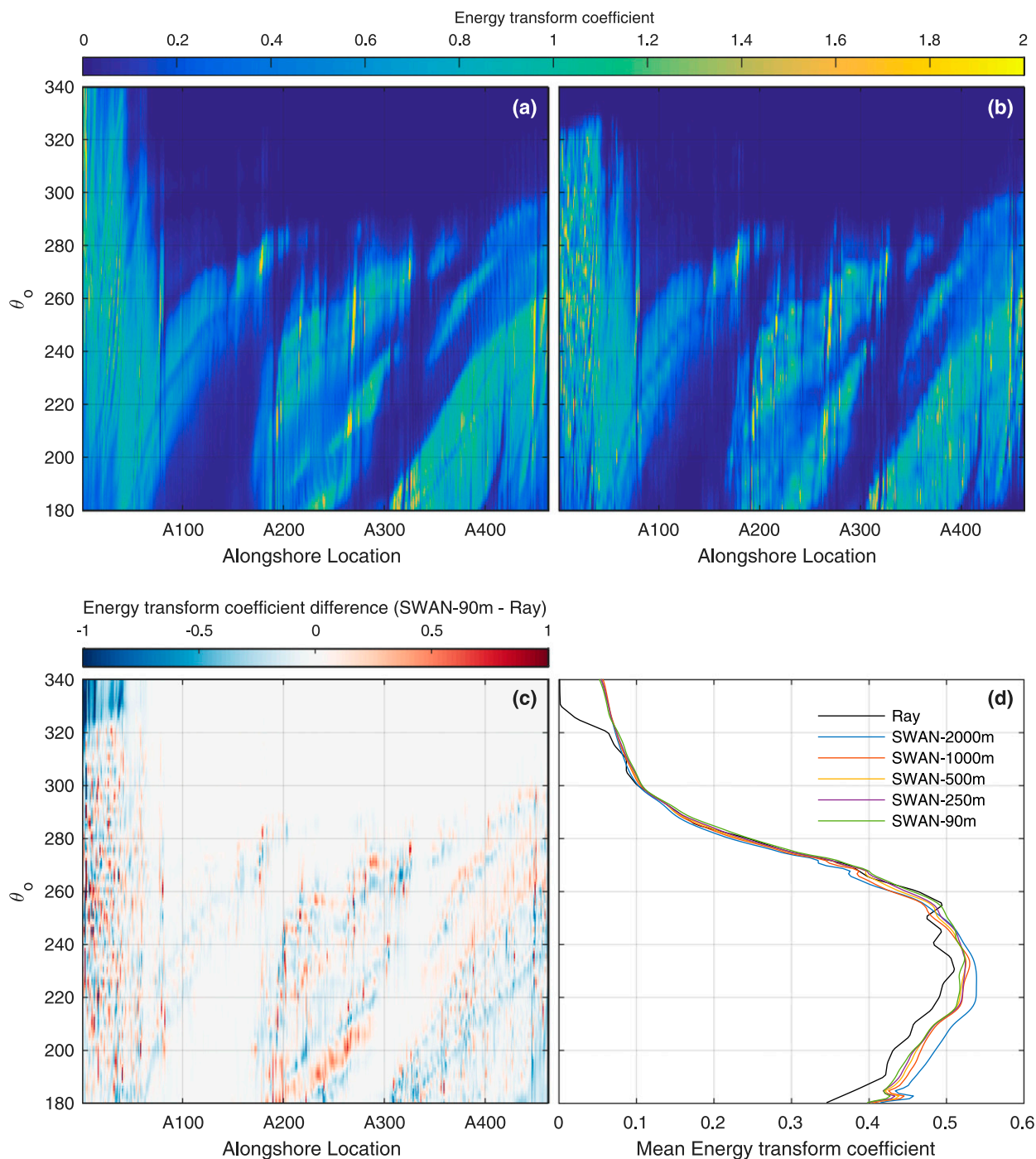
FIG. 3. Nearshore energy transfer coefficient at 0.07 Hz vs alongshore location (*x* axis) and offshore direction estimated from (a) high-resolution SWAN simulations (90 m) and (b) ray-tracing methods, and (c) their difference. (d) Transfer coefficients averaged over all alongshore locations for varying SWAN resolutions (see legend) and ray-tracing methods.

focusing regions. Alongshore energy transform co-efficients, integrated in 5° bins of offshore direction, vary significantly as the offshore direction changes. For example, as the offshore angle shifts 5° northward from 270°, the focusing near 119.5°W weakens, and

the strongest focusing offshore of Ventura, California, moves ~1 km alongshore (Fig. 4a). Coarse SWAN-derived coefficients tend to smooth alongshore variations and underestimate the focusing near Ventura (Fig. 4b). Overall, agreement is best between high-resolution
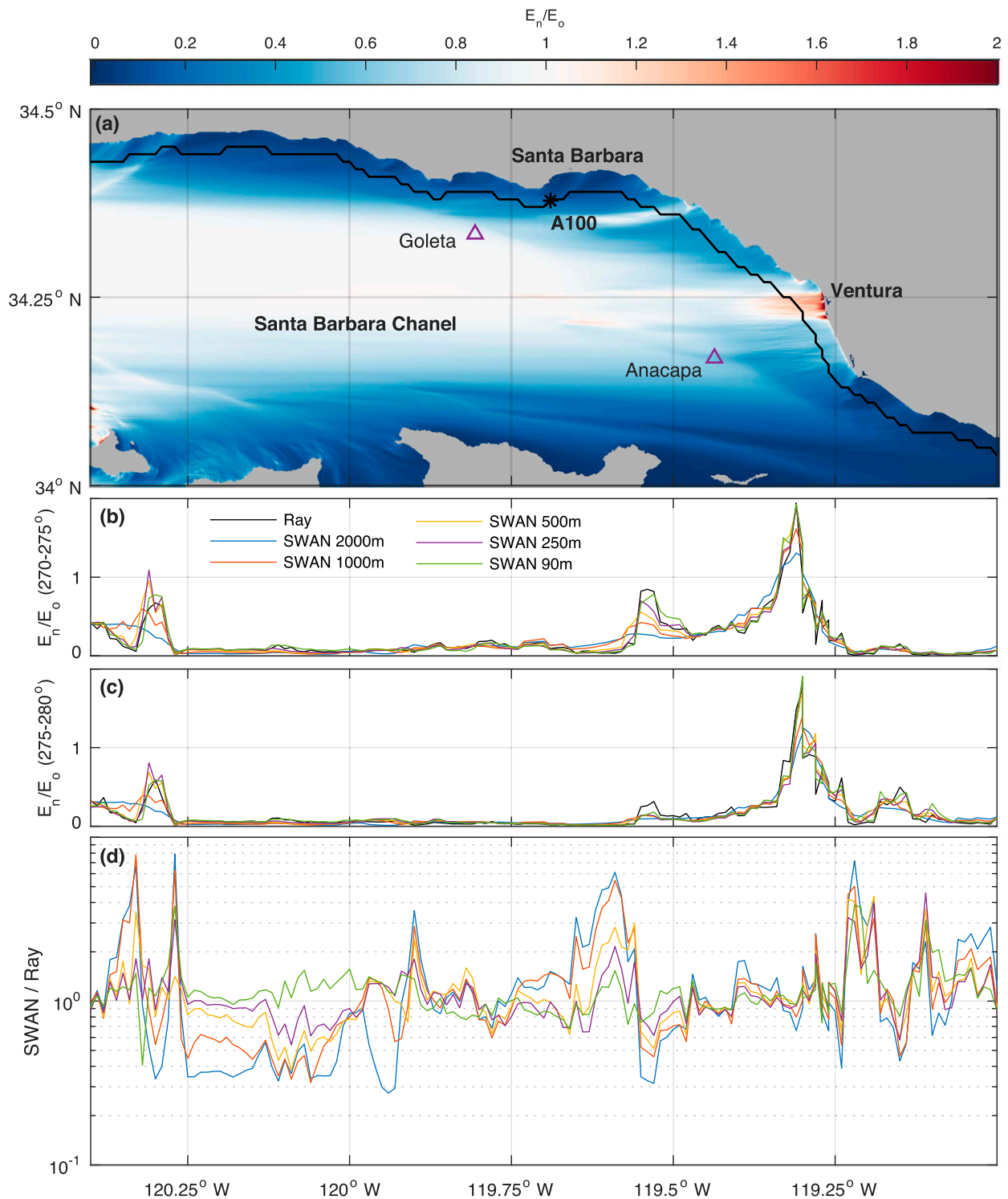
FIG. 4. Relative energy (a) in the Santa Barbara Channel for waves from 270° to 275° at 0.07 Hz, estimated from SWAN simulation at 90-m spatial resolution (color bar at top, red indicates focusing). (b),(c) Relative energy on the shallow black alongshore contour shown in (a), for (b) 270°–275°; and (c) 275°–280° offshore-direction bins using ray tracing (black) and SWAN (colors indicate resolutions, see legend). (d) Ratio of SWAN- and ray-derived coefficients for 270°–275° direction bins. Coarser SWAN resolutions tend to smooth out alongshore variations.
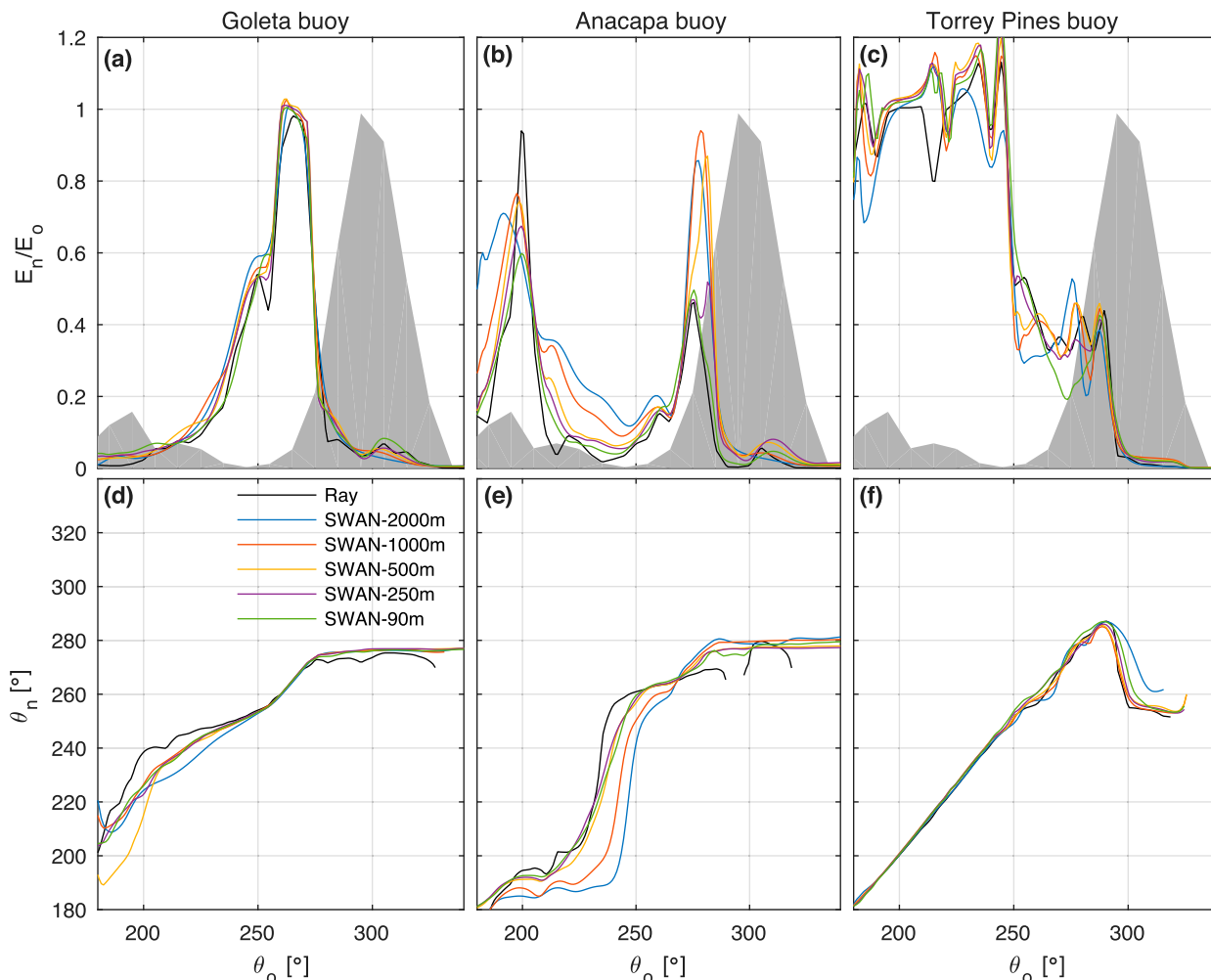
FIG. 5. (a)–(c) Nearshore energy transfer coefficients and (d)–(f) nearshore mean direction vs offshore direction for 0.07 Hz at (a),(d) Goleta, (b),(e) Anacapa, and (c),(f) Torrey Pines buoy locations derived by ray-tracing (black) and SWAN model simulations (colors). Gray shading shows relative mean offshore energy predicted by NOAA-WW3 hindcast. At the extremely sheltered Anacapa buoy site, higher-spatial-resolution simulations agree more closely with ray-tracing results.

SWAN- and ray-derived coefficients, indicating the importance of resolution in this sheltered region.

Transfer coefficients at buoy sites, with superposed offshore climatology, both shown as functions of offshore angle θ_o, illustrate the difficulty of predicting Southern California waves accurately. The directions of energetic offshore waves are largely blocked—all three buoy sites are sheltered from the dominant northwest swell at 300° (gray shading in Figs. 5a–c). Nearshore wave predictions are the product of both peak offshore energy with low transfer coefficients and relatively low offshore energy with large transfer coefficients. As such, accurate nearshore predictions demand accuracy at both low and high energy for transfer coefficients and offshore spectra $E_o(f, \theta_o)$.

Differences in transform coefficients tend to be largest at low energy. At Anacapa coarse SWAN simulations yield K over 2 times larger than ray-derived methods for the open sectors in the west (270°) and southwest (220°) directions (Fig. 5b). Overall, higher-resolution SWAN estimates are increasingly similar to ray-tracing methods; however, at some locations and directions, differences between the SWAN- and ray-derived coefficients persist. For example, at Anacapa peak energy transformation from 200° depends on several small islands and shows consistent discrepancy across varying SWAN resolutions (Fig. 5b). At more exposed locations (e.g., Torrey Pines buoy site), transfer coefficients are more similar and vary less at higher SWAN model resolutions (Fig. 5c), with the exception of some southwest directions. In general, smoother SWAN results are likely due to numerics.
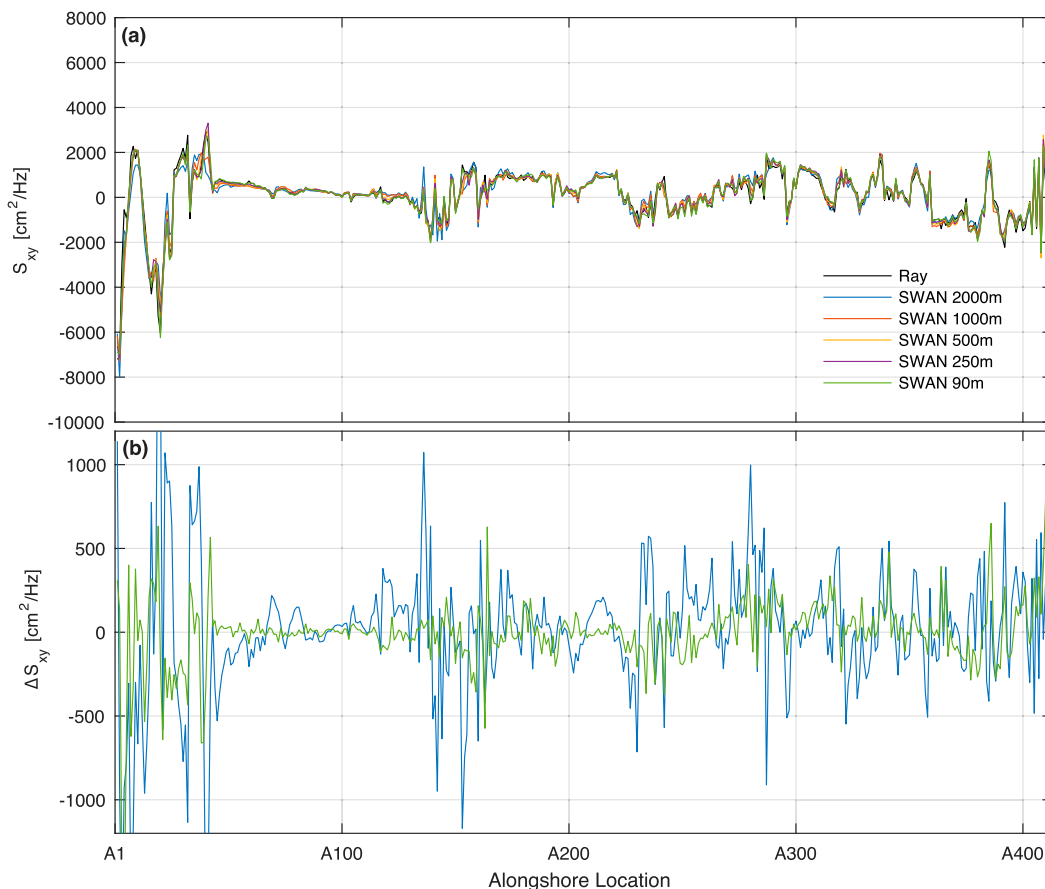
FIG. 6. (a) Predicted S_{xy} (local shore-normal coordinates) vs alongshore location for rays and different SWAN resolutions and (b) for 2000- and 90-m SWAN resolutions differenced with ray-derived S_{xy}, that is, $\Delta S_{xy} = S_{xy}^{\text{SWAN}} - S_{xy}^{\text{ray}}$.

Mean incident nearshore direction is also estimated as a function of offshore direction (Figs. 5d,e),

$$\overline{\theta_n}(\theta_o) = \arctan\left[\frac{K(i, f, \theta_o, \sin\theta_o)}{K(i, f, \theta_o, \cos\theta_o)}\right], \tag{5}$$

where setting $g(\theta) = \sin\theta$ and $g(\theta) = \cos\theta$ yields transfer coefficients for directional moments a_1 and b_1, respectively, from which mean direction $\overline{\theta_n}$ is estimated (Kuik et al. 1988). Similar to the comparison of energy transfer coefficients, mean direction estimates for energy arrival at offshore direction θ_o vary with changing SWAN model resolution. At sheltered locations, direction estimates vary more with model resolution, and high-resolution estimates are similar to ray-derived methods (Figs. 5d,e). At less sheltered locations, results are similar and vary less with model resolution (Fig. 5f). Directions are not estimated where the energy transfer coefficient is small (<0.5%) and estimates are unreliable.

To first order, alongshore transport (sediments, tracers) is proportional to the alongshore radiation stress S_{xy}

(Komar and Inman 1970; Guza et al. 1986), which is related to the directional moment b_2, such that

$$S_{xy} = \int\left(\frac{c_g}{c}\right)E(f)\,b_2(f)\,df, \tag{6}$$

where c is wave phase velocity and c_g is wave group velocity. Transfer coefficients for b_2, where $g(\theta) = \sin2\theta$, are rotated to shore normal coordinates relative to the local bathymetry gradient. Alongshore sediment transport is proportional to S_{xy}, and erosion and accretion theoretically depend on alongshore gradients of S_{xy}, the so-called divergence of the drift (e.g., CERC 1984a,b).

Mean S_{xy}, estimated from mean offshore wave conditions (Fig. 2) and SWAN- and ray-derived transfer coefficients, are similar alongshore (Fig. 6a). Differences between S_{xy} estimates are largest in Santa Barbara Channel (near A30) for northwest incident energy, and higher SWAN model resolutions are more similar to rays (Fig. 6b). Absolute mean differences across the
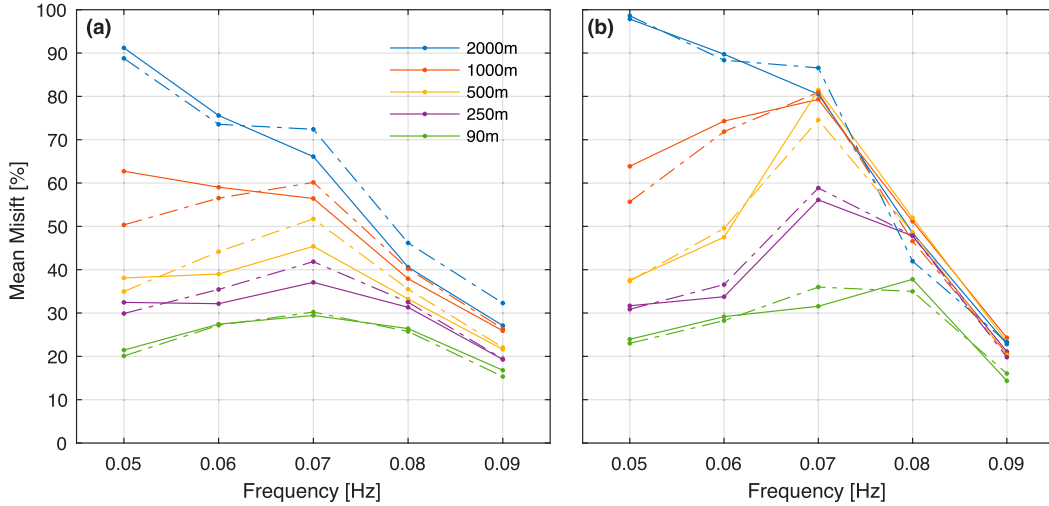
FIG. 7. (a) Mean and (b) climatological-weighted misfit (Fig. 2) between SWAN- and ray-derived transfer coefficients averaged across buoy locations vs swell-band frequency for first-order numerics (dashed–dotted) and second-order numerics (solid). Colors (see legend) indicate SWAN model spatial resolution.

region show the best agreement at the highest SWAN model resolution.

As shown above, misfit between SWAN- and ray-derived transfer coefficients is usually lower at higher SWAN model resolutions, consistent across swell-band frequencies. Climatological misfit is quantified as the total energy misfit (positive or negative) relative to the total incoming energy, weighted by mean offshore spectra $\overline{E_o}(f, \theta_o)$ in Fig. 2, where

$$\text{misfit} = 100 \frac{\int \overline{E_o}(\theta_o)|K_{\text{SWAN}}(\theta_o) - K_{\text{ray}}(\theta_o)|d\theta_o}{\int W(\theta_o)\,K_{\text{ray}}(\theta_o)\,d\theta_o}. \quad (7)$$

Mean misfit is averaged over all angles and is not weighted. Climatological and mean misfits, averaged across buoy locations, decrease with both increasing SWAN model resolution and frequency (Figs. 7a,b). Mean and offshore-climatology misfits show similar trends, with less separation at frequencies ≥ 0.07 Hz (Fig. 7b). Misfit at higher frequency is reduced because refraction weakens for these shorter wavelengths.

SWAN computations, by default, use second-order numerics (SORDUP); however, SWAN simulations were also run with first-order numerics (BSBT). With some exceptions, misfit to ray-derived transforms is slightly larger for first-order numerics, particularly at higher frequencies (Fig. 7a).

At individual buoys, wave height H_s predictions with spectra from the NOAA-WW3 hindcast vary for different transforms (Fig. 8). At 90-m resolution, the highest root-mean-square difference (RMSD) misfit is 4 cm between SWAN- and ray-derived transforms. At 1000- and 2000-m SWAN resolution, differences can double. The RMSD of H_s with 2000-m resolution at Anacapa and Torrey Pines is about 15% but with opposite sign (Figs. 8b,c). A simple calibration of coarse models would not improve the overall regional skill. During extreme wave events, the differences in wave heights exceed 0.5 m. (Fig. 8)

4. Summary

Swell (0.05–0.09 Hz) wave energy propagation is linearly modeled (shoaling, refraction, blocking) in Southern California (Fig. 1). Nearshore transfer coefficients (for energy, direction, and alongshore radiation stress) estimated with SWAN and ray-tracing techniques are similar as expected because they model identical physics, albeit with differing numerics. In sheltered regions, transform coefficients are sensitive to SWAN model spatial resolution. Higher-spatial-resolution SWAN model runs yield transfer coefficients most similar to ray-tracing techniques, while low-resolution estimates smooth alongshore variation (Fig. 4), biases some sheltered locations high (e.g., near Santa Barbara, California), biases others low (e.g., near San Diego, California), and impact alongshore forcing estimates (Fig. 6), as compared to higher-resolution estimates and ray-derived transforms (Fig. 1). Transfer coefficients vary most in highly sheltered regions such as the Santa Barbara Channel, where energy transfer
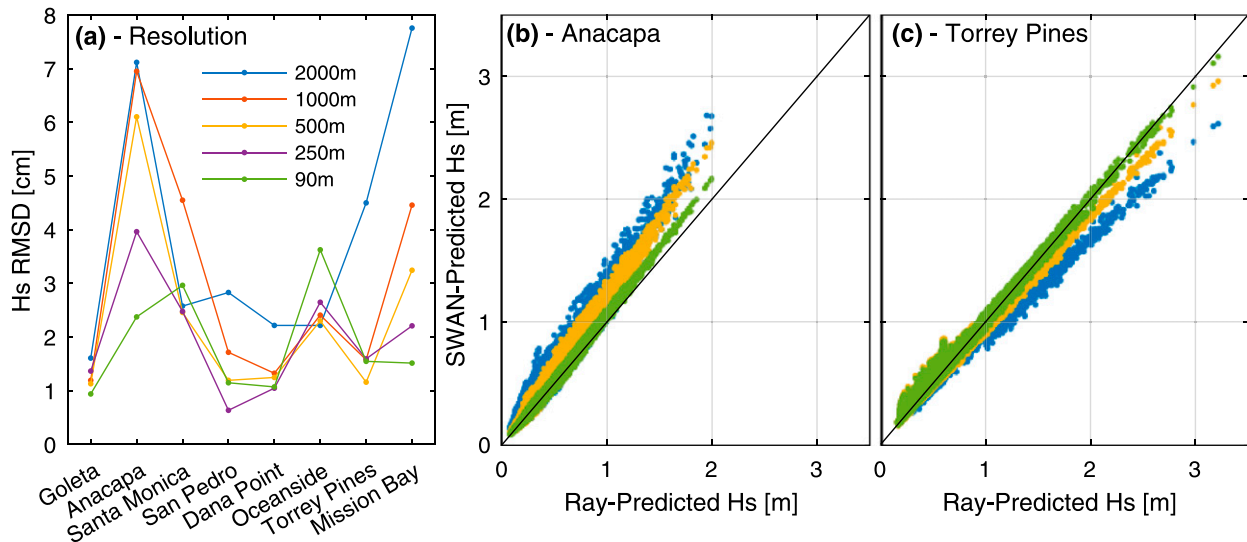
FIG. 8. Comparison of SWAN- and ray-derived wave height H_s predictions at buoy locations, initialized offshore with the 2000–09 WW3 spectra: (a) H_s RMSD vs buoy location, and SWAN- vs ray-predicted H_s at (b) Anacapa and (c) Torrey Pines. Crude (2000 m) resolution biases H_s about 15% high at Anacapa and 15% low at Torrey Pines (note E is biased about 30%).

estimates can vary by a factor of 2 between low and high SWAN model resolutions (Figs. 4,5). Low resolution typically results in relatively small differences in predicted average wave height, but during large events it may account for regional bias up to 0.5 m (Fig. 8). Linear wave transformation significantly reduces computation for long-term hindcasts or future climatologies and is similarly accomplished by SWAN and ray-tracing approaches.

SWAN is widely used and includes several important additional physical processes. By necessity, SWAN solves for wave transformation over the entire domain, which is convenient for some modeling tasks but impractical for large domains at high (say, 100 m or less) resolution, owing to memory and computational constraints. Ray tracing does not suffer from numerical diffusion, can work with large domains at high spatial resolution, and is ideal for rapidly generating swell wave transforms for a few nearshore locations (e.g., alongcoast transects in, say, 10- or 20-m depth). Additionally, ray parallelization is simplified because paths are independent. The domain, bathymetry, relevant physics, and locations of interest determine the inherent suitability of SWAN- or ray-derived transforms, or a combination of the two (e.g., rays at low frequency and SWAN at local sea frequencies). Finally, SWAN is well documented and user friendly with many readily available packages for processing inputs and outputs. Ray methods are not user friendly at the present time.

REFERENCES

Ardhuin, F., T. H. C. Herbers, and W. C. O'Reilly, 2001: A hybrid Eulerian–Lagrangian model for spectral wave evolution with application to bottom friction on the continental shelf. *J. Phys. Oceanogr.*, **31**, 1498–1516, https://doi.org/10.1175/1520-0485 (2001)031<1498:AHELMF>2.0.CO;2.

——, W. C. O'Reilly, T. H. C. Herbers, and P. F. Jessen, 2003a: Swell transformation across the continental shelf. Part I: Attenuation and directional broadening. *J. Phys. Oceanogr.*, **33**, 1921–1939, https://doi.org/10.1175/1520-0485(2003)033<1921: STATCS>2.0.CO;2.

——, T. H. C. Herbers, P. F. Jessen, and W. C. O'Reilly, 2003b: Swell transformation across the continental shelf. Part II: Validation of a spectral energy balance equation. *J. Phys. Oceanogr.*, **33**, 1940–1953, https://doi.org/10.1175/1520-0485 (2003)033<1940:STATCS>2.0.CO;2.

Booij, N., R. C. Ris, and L. H. Holthuijsen, 1999: A third-generation wave model for coastal regions: 1. Model description and validation. *J. Geophys. Res.*, **104**, 7649–7666, https:// doi.org/10.1029/98JC02622.

Camus, P., F. J. Mendez, and R. Medina, 2011: A hybrid efficient method to downscale wave climate to coastal areas. *Coastal Eng.*, **58**, 851–862, https://doi.org/10.1016/j.coastaleng.2011.05.007.

CERC, 1984a: Shore protection manual. Vol. I, Tech. Rep., U.S. Army Coastal Engineering Research Center, Corps of Engineers, 652 pp.

——, 1984b: Shore protection manual. Vol. II, Tech. Rep., U.S. Army Coastal Engineering Research Center, Corps of Engineers, 652 pp.

Chawla, A., D. M. Spindler, and H. L. Tolman, 2011: A thirty year wave hindcast using the latest NCEP Climate Forecast System Reanalysis winds. *Proc. 12th Int. Workshop on Wave Hindcasting and Forecasting and Third Coast Hazards Symp.*, Kohala Coast, HI, U.S. Army Corps of Engineers, I1, http://waveworkshop.org/12thWaves/papers/Kona11_Chawlaetal.pdf.

——, ——, and ——, 2013: Validation of a thirty year wave hindcast using the Climate Forecast System Reanalysis winds. *Ocean Modell.*, **70**, 189–206, https://doi.org/10.1016/j.ocemod.2012.07.005.

Crosby, S. C., W. C. O'Reilly, and R. T. Guza, 2016: Modeling long-period swell in Southern California: Practical boundary conditions from buoy observations and global wave model predictions. *J. Atmos. Oceanic Technol.*, **33**, 1673–1690, https://doi.org/10.1175/JTECH-D-16-0038.1.

——, B. D. Cornuelle, W. C. O'Reilly, and R. T. Guza, 2017: Assimilating global wave model predictions and deep-water wave observations in nearshore swell predictions. *J. Atmos. Oceanic Technol.*, **34**, 1823–1836, https://doi.org/10.1175/JTECH-D-17-0003.1.

Dorrestein, R., 1960: Simplified method of determining refraction coefficients for sea waves. *J. Geophys. Res.*, **65**, 637–642, https://doi.org/10.1029/JZ065i002p00637.

Gorrell, L., B. Raubenheimer, S. Elgar, and R. Guza, 2011: SWAN predictions of waves observed in shallow water onshore of complex bathymetry. *Coastal Eng.*, **58**, 510–516, https://doi.org/10.1016/j.coastaleng.2011.01.013.

Guza, R. T., E. Thorton, and N. Christensen Jr., 1986: Observations of steady longshore currents in the surf zone. *Bull. Amer. Meteor. Soc.*, **16**, 1959–1969, https://doi.org/10.1175/1520-0485(1986)016<1959:OOSLCI>2.0.CO;2.

Hegermiller, C. A., J. A. A. Antolinez, A. Rueda, P. Camus, J. Perez, L. H. Erikson, P. L. Barnard, and F. J. Mendez, 2017: A multimodal wave spectrum–based approach for statistical downscaling of local wave climate. *J. Phys. Oceanogr.*, **47**, 375–386, https://doi.org/10.1175/JPO-D-16-0191.1.

Komar, P., and D. Inman, 1970: Longshore sand transport on beaches. *J. Geophys. Res.*, **75**, 5914–5927, https://doi.org/10.1029/JC075i030p05914.

Kuik, A. J., G. P. van Vledder, L. H. Holthuijsen, A. J. Kuik, G. P. van Vledder, and L. H. Holthuijsen, 1988: A method for the routine analysis of pitch-and-roll buoy wave data. *J. Phys. Oceanogr.*, **18**, 1020–1034, https://doi.org/10.1175/1520-0485(1988)018<1020:AMFTRA>2.0.CO;2.

Kumar, N., D. L. Cahl, S. C. Crosby, and G. Voulgaris, 2017: Bulk versus spectral wave parameters: Implications on Stokes drift estimates, regional wave modeling, and HF radars applications. *J. Phys. Oceanogr.*, **47**, 1413–1431, https://doi.org/10.1175/JPO-D-16-0203.1.

Le Mehaute, B., and J. D. Wang, 1982: Wave spectrum changes on sloped beach. *J. Waterw. Port Coastal Ocean Div.*, **108**, 33–47.

Longuet-Higgins, M. S., 1957: On the transformation of a continuous spectrum by refraction. *Math. Proc. Cambridge Philos. Soc.*, **53**, 226, https://doi.org/10.1017/S0305004100032163.

——, D. Cartwright, and N. Smith, 1963: Observations of the directional spectrum of sea waves using the motions of a floating buoy. *Ocean Wave Spectra: Proceedings of a Conference*, Prentice-Hall, 111–136.

Menéndez, M., F. J. Méndez, I. J. Losada, and N. E. Graham, 2008: Variability of extreme wave heights in the northeast Pacific Ocean based on buoy measurements. *Geophys. Res. Lett.*, **35**, L22607, https://doi.org/10.1029/2008GL035394.

Munk, W., W. C. O'Reilly, and J. Reid, 1988: Australia–Bermuda sound transmission experiment (1960) revisited. *J. Phys. Oceanogr.*, **18**, 1876–1898, https://doi.org/10.1175/1520-0485(1988)018<1876:ABSTER>2.0.CO;2.

O'Reilly, W. C., and R. T. Guza, 1991: Comparison of spectral refraction and refraction-diffraction wave models. *J. Waterw. Port Coastal Ocean Eng.*, **117**, 199–215, https://doi.org/10.1061/(ASCE)0733-950X(1991)117:3(199).

——, and ——, 1993: A comparison of two spectral wave models in the Southern California Bight. *Coastal Eng.*, **19**, 263–282, https://doi.org/10.1016/0378-3839(93)90032-4.

——, and ——, 1998: Assimilating coastal wave observations in regional swell predictions. Part I: Inverse methods. *J. Phys. Oceanogr.*, **28**, 679–691, https://doi.org/10.1175/1520-0485(1998)028<0679:ACWOIR>2.0.CO;2.

——, C. B. Olfe, J. Thomas, R. Seymour, and R. Guza, 2016: The California coastal wave monitoring and prediction system. *Coastal Eng.*, **116**, 118–132, https://doi.org/10.1016/j.coastaleng.2016.06.005.

Portilla-Yandún, J., L. Cavaleri, and G. P. Van Vledder, 2015: Wave spectra partitioning and long term statistical distribution. *Ocean Modell.*, **96**, 148–160, https://doi.org/10.1016/j.ocemod.2015.06.008.

Rijnsdorp, D. P., P. B. Smit, and M. Zijlema, 2014: Non-hydrostatic modelling of infragravity waves under laboratory conditions. *Coastal Eng.*, **85**, 30–42, https://doi.org/10.1016/j.coastaleng.2013.11.011.

Rogers, W. E., J. M. Kaihatu, H. A. Petit, N. Booij, and L. H. Holthuijsen, 2002: Diffusion reduction in an arbitrary scale third generation wind wave model. *Ocean Eng.*, **29**, 1357–1390, https://doi.org/10.1016/S0029-8018(01)00080-4.

——, ——, L. Hsu, R. E. Jensen, J. D. Dykes, and K. T. Holland, 2007: Forecasting and hindcasting waves with the SWAN model in the Southern California Bight. *Coastal Eng.*, **54**, 1–15, https://doi.org/10.1016/j.coastaleng.2006.06.011.

Tolman, H. L., 2009: User manual and system documentation of WAVEWATCH-III version 3.14. NOAA Tech. Note, MMAB Contribution 276, 220 pp., http://polar.ncep.noaa.gov/mmab/papers/tn276/MMAB_276.pdf.

Young, I., S. Zieger, and A. V. Babanin, 2011: Global trends in wind speed and wave height. *Science*, **332**, 451–455, https://doi.org/10.1126/science.1197219.